Surface & Coatings Technology 447 (2022) 128880

Contents lists available at ScienceDirect

Surface & Coatings Technology

journal homepage: www.elsevier.com/locate/surfcoat

Effect of processing conditions on residual stress in sputtered transition metal nitrides (TiN, ZrN and TaN): Experiments and modeling

Zhaoxia Rao [a,d,*], Tong Su [a], Thomas Koenig [b], Gregory B. Thompson [b], Diederik Depla [c], Eric Chason [a]

[a] School of Engineering, Brown University, Providence, RI 02912, United States of America
[b] Department of Metallurgical & Materials Engineering, The University of Alabama, Tuscaloosa, AL 35487, United States of America
[c] Department for Solid State Sciences, Ghent University, Krijgslaan 281 (S1), 9000 Ghent, Belgium
[d] Applied Materials Inc., 974 Arques Avenue, Sunnyvale, CA 94085, United states of America

ARTICLE INFO

Keywords:
Thin films
Residual stress
Sputtering deposition

ABSTRACT

Stress evolution during reactive DC magnetron sputtering deposition in TiN, ZrN and TaN films at different growth rates, pressures and relative gas flow rates was measured by a wafer curvature technique. The results indicate that, for a given growth rate, the stress in each material is tensile at higher pressures and becomes more compressive with lower pressures. At lower pressures, the stress tends to become more compressive with increasing growth rate. Increasing the gas flow rate of N_2 relative to Ar is observed to enhance compressive stress generation in TaN but has a weaker effect on TiN and ZrN. At lower pressure, the compressive stress magnitude scales with TiN < ZrN < TaN. The stress at different processing conditions was analyzed in terms of a kinetic model that includes the effects of growth kinetics and energetic bombardment. The resulting parameters are compared with calculations from binary collision Monte-Carlo simulation codes.

1. Introduction and background

Transition metal nitride films have wide applications such as hard coatings, diffusion barriers and optical coatings because of their exceptional physical properties including high hardness, mechanical strength, and chemical inertness [1–4]. However, the stress induced during the film deposition can lead to deformation or cracks [5,6], which adversely affects the performance and lifetime of the devices it is used in. Therefore, it is of critical importance to understand the factors that control the stress in metal nitride films.

Stress evolution in sputtered metal-nitride films at different processing conditions has been reported previously [7–12]. Metal-nitride films are often deposited by reactive sputter deposition using a DC magnetron source. The characteristics of the particles impinging on the sample depend on the processing conditions in the chamber. In particular, a lower pressure leads to an increase in energy of the incoming particles by a reduction of their scattering while higher power leads to an increase in the deposition rate. The gas consists of a combination of Ar and N_2 in which the Ar remains inert while the N_2 reacts with the metal to form the nitride. Altering the gas flow rates alters the relative fluxes of the two species that arrive on the target. In general, the stress is found to become less tensile/ more compressive when the pressure is decreased for a constant growth rate. In TiN [12], the incremental stress changes from 0.30 to −1.55 GPa when the pressure is decreased from 0.55 to 0.32 Pa. Similarly, in ZrN [8], the incremental stress changes from 0.40 to −6.5 GPa with a decrease in pressure from 0.42 to 0.13 Pa. This is generally attributed to the increase in particle energy at lower pressure, due to fewer collisions in the gas [13]. The dependence on growth rate is often coupled to the pressure. For both TiN and ZrN [7], when the pressure is high the stress remains tensile when the growth rate increases. On the other hand, at low pressure the stress becomes more compressive when the growth rate is increased.

The effect of gas flow rates on stress in nitride films has also been reported [10–12]. In the work from Abadias et al. [12], stress in TiN is measured when the N_2 flow rate is varied in the range of 0–18 sccm with a total gas pressure of 0.30 Pa. The stress is found to be more tensile at a lower N_2 flow rate and more compressive at a higher N_2 flow. The stress change correlates with a change in texture from pronounced (111) texture to pure (002) texture. They estimate that the film also has a smaller grain size at the higher N_2 flow rate based on XRD analysis.

* Corresponding author at: Applied Materials Inc., 974 Arques Avenue, Sunnyvale, CA 94085, United States of America.
E-mail address: zhaoxiarao.materials@gmail.com (Z. Rao).

https://doi.org/10.1016/j.surfcoat.2022.128880
Received 17 June 2022; Received in revised form 27 August 2022; Accepted 4 September 2022
Available online 11 September 2022
0257-8972/© 2022 Elsevier B.V. All rights reserved.

Huang et al. [11] measured stress in ZrN by a modified XRD $sin^2\psi$ method. The measured stress decreases with the increase of N_2 flow rate and then increases with the further increase of the N_2 flow rate in the range of N_2 flow rates from 5 to 35 sccm with a fixed Ar flow rate of 10.4 sccm. They suggest this might be due to the defects created by Zr ions (i.e., more defects created with the increase of N_2 flow rate at the lower flow rate regime, but with the further increase of N_2 flow rate, the defects become less due to the kinetic energy loss of Zr ion by the increased collisions with gaseous particles). The grain sizes range from 15 to 30 nm, with the grain size decreasing with the increasing N_2 flow rate. Zaman et al. [10] reported that the stress in Ta—N films ranges from −2.67 to −0.20 GPa for films deposited with a total gas flow rate of 25 sccm and N_2 content varied from 25 % to 3 %. They ascribe the lower stress at lower N_2 gas flow rate to the mixed phases (fcc TaN and hexagonal Ta_2N) in the film.

Previously published work on stress in sputtered films has reported that the processing conditions (i.e., growth rate [14–16], pressure [6,8,12,17–22], substrate bias voltage [21,23–26]) and microstructure [27] can have a significant effect. This suggests an approach to control the stress by tailoring the deposition parameters. However, the dependence on different parameters, and interactions among the different parameters can make this complex. Developing a useful understanding requires comprehensive measurements that systematically considers the effect of each of multiple parameters. Consequently, the current work reports on a series of measurements that quantify the effect of several processing parameters (growth rate, pressure and relative gas flow rates) on the stress, phase formation and grain size in sputtered metal-nitride films of different composition(TiN, ZrN, and TaN). The results are discussed in terms of a previously developed kinetic model [28], and the parameters are compared with calculations from binary-collision Monte-Carlo simulations (SRIM [29] and SIMTRA [30]).

2. Experiments and simulations

2.1. Experiments

The TiN, ZrN and TaN films were deposited at ambient temperature onto a [100] Si substrate via DC magnetron reactive sputtering. The in-plane dimension of the Si wafer is approximately 30 × 10 mm and the thickness ranges from 0.175 mm to 0. 285 mm. The Si wafer was cleaned via ultrasonic agitation in the successive baths of acetone, methanol, isopropanol for 5 min each before deposition and followed by drying with compressed N_2 gas before deposition. The substrate was electrically grounded and located 18 cm away from the target. The experiments were conducted by using 3″ diameter metallic targets Ti (99.995 % pure), Zr (99.2 % pure), and Ta (99.95 % pure). The base pressure prior to sputtering was less than 4×10^{-5} Pa. The pressure in the chamber during the deposition process is measured by a Pirani gauge. The sputtering deposition was performed under constant power mode. Before deposition, the target was pre-sputtered in the pure Ar gas atmosphere at a flow rate of 15 sccm for 10 min to remove the contamination on the target surface. The growth rate was adjusted between depositions by changing the power.The total gas pressure was controlled by changing the pumping speed via a throttle valve. The growth rate was monitored by a quartz sensor during the deposition, and the actual growth rate was corrected by using ellipsometry. The nitride films were deposited in a mixture of Ar and N_2 gas. The flow rate of Ar was kept constant at 26 sccm while the flow rate of N_2 was varied from 6 to 10 sccm for TiN and 3 to 10 sccm for ZrN and TaN. The flow rate ratios are denoted in the text as 26/X sccm where the Ar flow rate is 26 sccm and the N_2 flow rate is X sccm. The range of gas flow rates was chosen to ensure that the deposited films have a cubic structure. The pressure and growth rate range for each material at each flow rate is listed in Table 1.

The real-time stress evolution in the TiN, ZrN and TaN films was measured using a wafer curvature technique [31,32] during the film deposition. In this method, a laser beam passes through an etalon to generate parallel beams which hit the sample and then be reflected to a CCD camera which records the spacing of the adjacent beams, thus providing curvature measurements of the sample during film deposition. The measured curvature is related to the product of stress and film thickness by using Stoney's equation [33]:

$$\kappa = \frac{6\bar{\sigma}h_f}{M_s h_s^2} \tag{1}$$

where $\bar{\sigma}$ is the stress averaged over the thickness of the film, h_f, h_s and M_s are the thickness and bi-axial modulus of the substrate, respectively. The product of stress and film thickness ($\bar{\sigma}h_f$) is often referred to as stress-thickness or force per width (F/w). The stress-thickness is calculated by integrating the stress throughout the film:

$$\bar{\sigma}h_f = \int_0^{h_f} \sigma(z)dz \tag{2}$$

where z is the direction perpendicular to the substrate and $\sigma(z)$ is the stress at a height of z above the film/substrate interface. If the stress in the previously deposited layers does not change, then the slope of the stress-thickness vs. film thickness is equal to the incremental stress, i.e., the stress in newly-deposited layers. This is also referred to as the steady-state stress if the grain size does not change with thickness.

The effects of processing conditions are quite complex since a change of one parameter can also lead to changes in other parameters such as texture or grain size which may also affect the stress. The experiments were therefore designed to investigate the effect of processing conditions systematically and quantitatively. Series of measurements were performed by changing one processing condition while keeping others constant (i.e., change growth rate while keeping the pressure and gas flow rates constant).

Specifically, the stress measurements were performed for each material by growing a sequence of layers at different growth rates for a constant pressure and gas flow rate ratio. For example, a sequential growth of TaN (after the buffer layer) at different growth rates at a pressure of 1 Pa and gas flow rate ratio of 26/6 sccm Ar/N_2 is shown in Fig. 1. The measured stress thickness at each growth interval is shown in Fig. 1 b) and the corresponding growth rate is shown in Fig. 1 a). The shaded grey areas are the pauses when the deposition was briefly interrupted. The stress-thickness does not change during pauses, indicating that the stress relaxation is minimal. Similar behavior was observed in the work by Abadias et al. [34].

The growth rate was ramped to a new value shortly after the pause and then rapidly became stable. The stress-thickness evolution was observed to be relatively linear during the growth at each growth rate. In addition, repeating the same growth-rate measurements at larger thicknesses shows the slope returns to the same as in the earlier measurement. These observations indicate that the grain size is not changing significantly with the film thickness, because if it were then the measured stress would also be changing with thickness [31]. Similar behavior has been observed in electrodeposited Ni [35]. Therefore, the slope of the stress-thickness measurements made for different intervals provides the steady-state stress for different processing conditions at a constant grain size.

Table 1
The processing condition investigated in the experiments for TiN, ZrN and TaN.

Material	Ar/N2 flow rate	Pressure range	Growth rate range
TiN	26/6 sccm	0.13–0.40 Pa	0.009–0.124 nm/s
	26/10 sccm	0.13–0.40 Pa	0.018–0.151 nm/s
ZrN	26/3 sccm	0.13–0.67 Pa	0.042–0.339 nm/s
	26/6 sccm	0.13–0.67 Pa	0.042–0.187 nm/s
	26/10 sccm	0.13–1.00 Pa	0.042–0.134 nm/s
TaN	26/3 sccm	0.40–1.00 Pa	0.038–0.464 nm/s
	26/6 sccm	0.40–1.00 Pa	0.031–0.464 nm/s
	26/10 sccm	0.40–1.60 Pa	0.039–0.335 nm/s

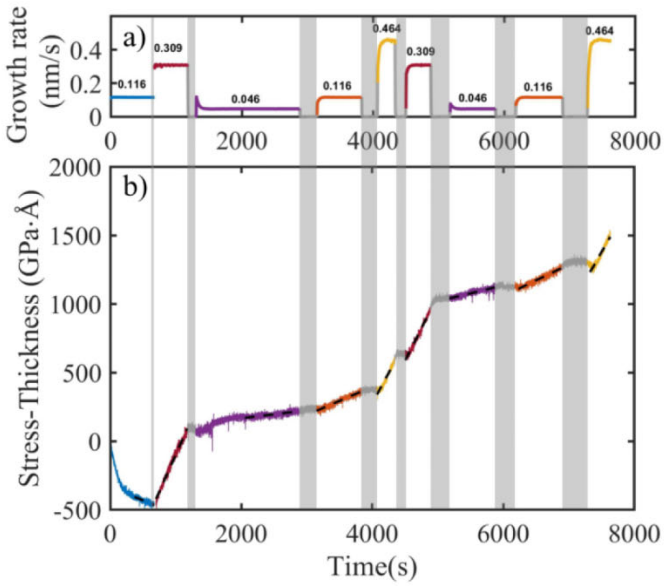

Fig. 1. Stress evolution of TaN films with sequential growth at multiple growth rates under a pressure of 1 Pa and gas flow rate ratio of 26/6 sccm Ar/N_2. The initial layer in the film growth was deposited at a pressure of 0.67 Pa and a growth rate of 0.116 nm/s as a buffer layer. a) growth rate and b) stress-thickness corresponding to each growth interval. The shaded grey areas are the pauses when the film deposition was turned off. The different colors correspond to different growth rates as indicated in the figure.

This method is used to develop a comprehensive set of stress measurements for TiN, ZrN and TaN films at different growth rates, pressures and flow rate ratios. The same growth conditions were repeated several times in each series of measurements to make sure the results were repeatable and to determine the experimental error. This allows an average value of steady-state stress to be associated with each growth rate, pressure, and set of gas flow rates. To ensure that the layers started with the same microstructure for each material, a buffer layer with nominal film thickness of 100 nm was initially deposited at the same condition on each sample for each material. The buffer layer for TiN was deposited at a pressure of 0.13 Pa and a growth rate of 0.089 nm/s and gas flow rate ratio of 26/6 sccm Ar/N_2; the buffer layer of ZrN was deposited at a growth rate of 0.085 nm/s and a pressure of 0.40 Pa and gas flow rate ratio of 26/6 sccm Ar/N_2 for ZrN; the buffer layer of TaN was deposited at a growth rate of 0.116 nm/s and a pressure of 0.67 Pa and gas flow rate ratio of 26/6 sccm Ar/N_2.

After deposition, the grain size in several of the films was characterized by cross-sectional transmission electron microscopy (TEM) using Tescan Lyra XMU dual-beam SEM-FIB to lift-out the samples. To determine the texture and phase of the different films, TiN, ZrN and TaN films were deposited on Si substrates at different growth rates, pressures and flow rate ratios. X-ray diffraction (XRD) measurements were made using a Bruker D8 Discovery High-resolution X-Ray Diffractometer in the Bragg-Brentano configuration.

2.2. Simulations

2.2.1. Kinetic model

To understand the effects of growth rate (R), pressure (P) and flow rate ratios on the steady-state stress in sputter-deposited nitride films, we use a previously developed kinetic model which includes the effect of growth kinetics and energetic bombardment. Details of the kinetic model can be found in previously published work [28]. Only a brief description of it is given here.

The kinetic model considers the effect of kinetic growth (non-energetic) and energetic effects due to the incorporation of adatoms near the grain boundary and defect creation in the bulk of the film as described by Eq. (3):

$$\sigma_{ss}^{sputt} = \sigma_C + (\sigma_T - \sigma_C)e^{\left(-\frac{\beta D}{RL}\right)} + A_0 \times \frac{l}{L} + \left(1 - \frac{l}{L}\right)\frac{B_0}{\left(1 + \frac{l}{R\tau_s}\right)} \quad (3)$$

The compressive stress in the model is assumed to be induced by the diffusion of adatoms from the surface into the grain boundaries driven by the non-equilibrium condition at the surface [36] (fitting parameter σ_C). Tensile stress (fitting parameter σ_T) is generated by the formation of a new grain boundary at the triple junction where two adjacent grains coalesce based on a mechanism proposed by Hoffman [37]. It is predicted to depend inversely on the square root of the grain size. The balance between tensile and compressive stress is determined by the kinetic parameter βD to describe the resulting stress during non-energetic growth [38]. L is the grain size in the film which is assumed to remain constant for steady-state conditions. The mechanisms in this model, with the addition of stress from grain growth, have been used to analyze stress in metal films deposited by electrodeposition [35,39–42] and evaporation [43,44].

The remaining terms describe stress-inducing mechanisms in energetic deposition. The third term on the right-hand side describes the stress generated by collision induced densification near the grain boundaries [45]. A_0 is an adjustable parameter that depends on growth rate, pressure and flux of energetic species. We assume the ratio of the flux of energetic species to deposited species (growth rate) does not change with growth rate, i.e., that the yield of backscattered atoms and sputtered particles does not change with growth rate for each pressure and set of gas flow rates. This is valid for sputtering of metals, but it may not be strictly true for nitrides where poisoning of the target occurs and can alter this ratio. However, since we are not able to measure the ratio of energetic species to deposited species, we assume that A* does not depend on the growth rate for each set of pressure and flow rate conditions. The fraction of the energetic particles that induce stress near the grain boundary is approximated to be proportional to $\frac{l}{L}$ where l is the implantation depth of defects created by energetic particles.

The fourth term describes the stress induced by the incorporation of defects in the remainder of the film. B_0 is an adjustable parameter that is related to the number of defects created per incident particle and the stress induced per defect. τ_s is the characteristic time for a defect to diffuse from the implantation depth l to surface. Since growing the surface is moving up at a rate R, $\tau_s$can be determined from

$$\sqrt{D_i \tau_s} = l + R\tau_s \quad (4)$$

where D_i is the diffusivity coefficient of defects. The energetic model has been used to analyze the stress in sputter deposited metals including Mo [28], Cu [13], Ni [46] and Ta [47].

2.2.2. Binary collision Monte-Carlo simulations

To understand the energetic effects in sputtered nitride films, we used computer simulations to model the incident particle energy, flux and resulting defect production during deposition under different conditions. The average energy of the sputtered and backscattered atoms that arrive at the substrate and the implantation depth of each species in the film were calculated using binary collision Monte-Carlo simulations (SRIM [29] and SIMTRA [30]). The sputter yield, backscatter yield, and angular and energy distribution of sputtered atoms and backscattered atoms were obtained from SRIM. The damage type used in the simulation was surface sputtering/ monolayer collision steps. Since SRIM is not able to simulate the bombardment of Ar^+ and N^+ on metal target simultaneously, separate simulations of Ar^+ or N^+ hitting the metal target were performed. In the simulation, we assume that the chemical composition on the target surface is not changed which might overestimate the sputter yield and backscatter yield because the target

poisoning effect will lower the average mass of the surface atoms in the reactive sputtering process. As the discharge voltage changes with the growth rate in the experiments mainly due to target poisoning, individual discharge voltages from each data set were used to do the calculation. The simulation results indicate that the average energy per sputtered atom and the ratio of the flux of backscattered neutrals to the flux of sputtered atoms are weakly dependent on discharge voltage, so the average discharge voltage is adequate for the calculations. The simulation was calculated by using 6 x 10^5 Ar^+ with incident energy of 340 eV or 6 x 10^5 N^+ with energy of 170 eV [48] (taken as half of the energy of Ar+). The incident energy of Ar^+ ions was taken as 75 % of the average target discharge voltage, considering the charge transfer collisions in the plasma sheath [49]. The threshold energy of atomic displacement in Ti, Zr, and Ta lattice was set as 30, 40, and 80 eV, respectively, referencing the work from Abadias [9,48] and the reference wherein it [50].

The results for the sputter yield, backscatter yield and the ratio (α) of the flux of backscattered atoms to the flux of sputtered atoms of Ti, Zr, and Ta by the bombardment of Ar^+ ions and N^+ ions are shown in Table 2a) and b), respectively.

The initial angular and energy distribution of sputtered and backscattered atoms obtained from SRIM calculations are used as input in SIMTRA to obtain the average energy of each species that arrives at the substrate. SIMTRA is a Monte Carlo program which simulates the transport of energetic atoms during sputtering deposition. In the program, the geometry of the experimental chamber is used. In this work, a Molière screened Coulomb potential was selected to describe the metal-gas interaction. An axial symmetric racetrack was used to sample the initial position of the simulated particles without considering the shape and depth of the target as the program assumes that the target surface is completely flat. Sputtered and backscattered particles are simulated separately in the program by using the initial energy and angular distribution of each species leaving the target from SRIM. The average energy of the deposited species [9] is estimated as:

$$\overline{E} = \frac{E_s^{Ar} \times Y_{sput,Ar} \times f_{Ar} \times t_s^{Ar} + E_s^N \times Y_{sput,N} \times f_N \times t_s^N + E_{bs}^{Ar} \times \beta_{Ar} \times f_{Ar} \times t_{bs}^{Ar} + E_{bs}^N \times \beta_N \times f_N \times t_{bs}^N}{Y_{sput,Ar} \times f_{Ar} \times t_s^{Ar} + Y_{sput,N} \times f_N \times t_s^N + \beta_{Ar} \times f_{Ar} \times t_{bs}^{Ar} + \beta_N \times f_N \times t_{bs}^N} \tag{3.7}$$

where $Y_{sput,\,Ar}$ and $Y_{sput,\,N}$ are the sputter yield of Ar and N, respectively. β_{Ar} and β_N are backscatter yield of Ar and N, respectively. f_{Ar} and f_N are the fraction of Ar^+ ion and N^+ ions in the chamber, respectively. And $f_{Ar} = \frac{N_{Ar}}{(N_{Ar}+2N_{N_2})}$, $f_N = \frac{2N_{N_2}}{(N_{Ar}+2N_{N_2})}$. t_s^i ($i = Ar^+ or\ N^+$) is the fraction of sputtered atom arrived at the substrate. t_{bs}^i ($i = Ar^+ or\ N^+$) is the fraction of backscattered atoms arrived at the substrate. They have been estimated by the relative flow rate of each gas species in the chamber. E_s^i ($i = Ar^+ or\ N^+$) is the average energy of the sputtered atoms by the bombardment of $i = Ar^+ or\ N^+$ ions. $E_{bs}^i (i = Ar^+ or\ N^+)$ is the average energy of backscattered atoms by the bombardment of $i = Ar^+ or\ N^+$ ions.

The implantation depths of each species were estimated by using SRIM. The damage type used in the simulation was detailed calculation with full damage cascade and the initial energy was set as the arriving energy of each species at the substrate calculated by SIMTRA.

Table 2
Sputter yield, backscatter yield and the ratio of the flux of sputtered atoms to the flux of backscattered atoms by the bombardment of a) Ar^+ and b) N^+ to the Ti, Zr and Ta metallic targets.

Materials	Sputter yield	Backscatter yield	α
a)			
Ti	0.4714	0.0261	0.0554
Zr	0.5904	0.1315	0.2228
Ta	0.4932	0.2591	0.5253
b)			
Ti	0.3135	0.1684	0.5371
Zr	0.2025	0.2921	1.4423
Ta	0.1192	0.3961	3.3232

3. Results

3.1. Steady-state stress for different processing conditions

The steady-state stress was determined by taking the slope of the stress-thickness measurements vs. thickness for each interval of growth under different conditions. The results for TiN, ZrN and TaN at different growth rates, pressures and flow rate ratios are shown in Fig. 2. Each panel shows the steady-state stress vs. growth rate for different pressures, as indicated in the legend. Each row corresponds to a different material (TiN, ZrN and TaN) from top to bottom. Each column corresponds to different flow rate ratios (26/3, 26/6 and 26/10 sccm) from left to right. The solid (or dashed) lines in the figure represent the fits to the kinetic model described in Section 4.1. The error bars in the figure were calculated by taking the standard deviation of all the measurements performed at the same processing conditions.

From the results, we can observe that in each material, for each growth rate, the stress is more compressive at lower pressure and more tensile at higher pressure. When the pressure is sufficiently high, the stress becomes independent of pressure as shown by the results in ZrN films. This can be explained by the reduced energy of the particles under higher pressure at which the particles experience more collisions during the transport from the target to the substrate. Tensile stress has been typically observed at higher pressure due to the formation of voids as reported in the literature [22,34]. At lower pressures, where the energetic effects are more significant, the magnitude of compressive stress in the deposited nitride films follows the trend that TaN > ZrN > TiN. This can be explained by the higher fraction of backscattered neutrals reaching substrate from Ta as indicated by Table 2.

3.2. Microstructural characterization

A buffer layer was deposited at the same processing condition for each materials (i.e., TiN buffer layer for TiN growth, ZrN buffer layer for ZrN growth, TaN buffer layer for TaN growth) to ensure that the growth layer was started with similar microstructure conditions. The average grain sizes for TiN, ZrN and TaN films were measured on some representative samples after they were deposited with multiple growth rates. The values for the grain sizes are 14 ± 10 nm, 11 ± 9 and 9 ± 6 nm, respectively. The error bars are estimated from measurements of different regions in the same sample, not across different samples. TEM also confirmed that the grain size does not change significantly with thickness, consistent with the results of the stress measurements.

XRD was performed in order to determine the texture and phase of the films for different processing conditions for each material (shown in Fig. 3). The XRD characterization was performed on samples that were deposited with multiple growth rates as described in Fig. 1 at each pressure and gas flow ratio. The thickness of the samples ranges from 425 to 1006 nm. The XRD patterns of the Si substrate without any deposition were scanned as a reference to analyze the patterns of the nitride films which is shown as the black curves in Fig. 3, indicating that

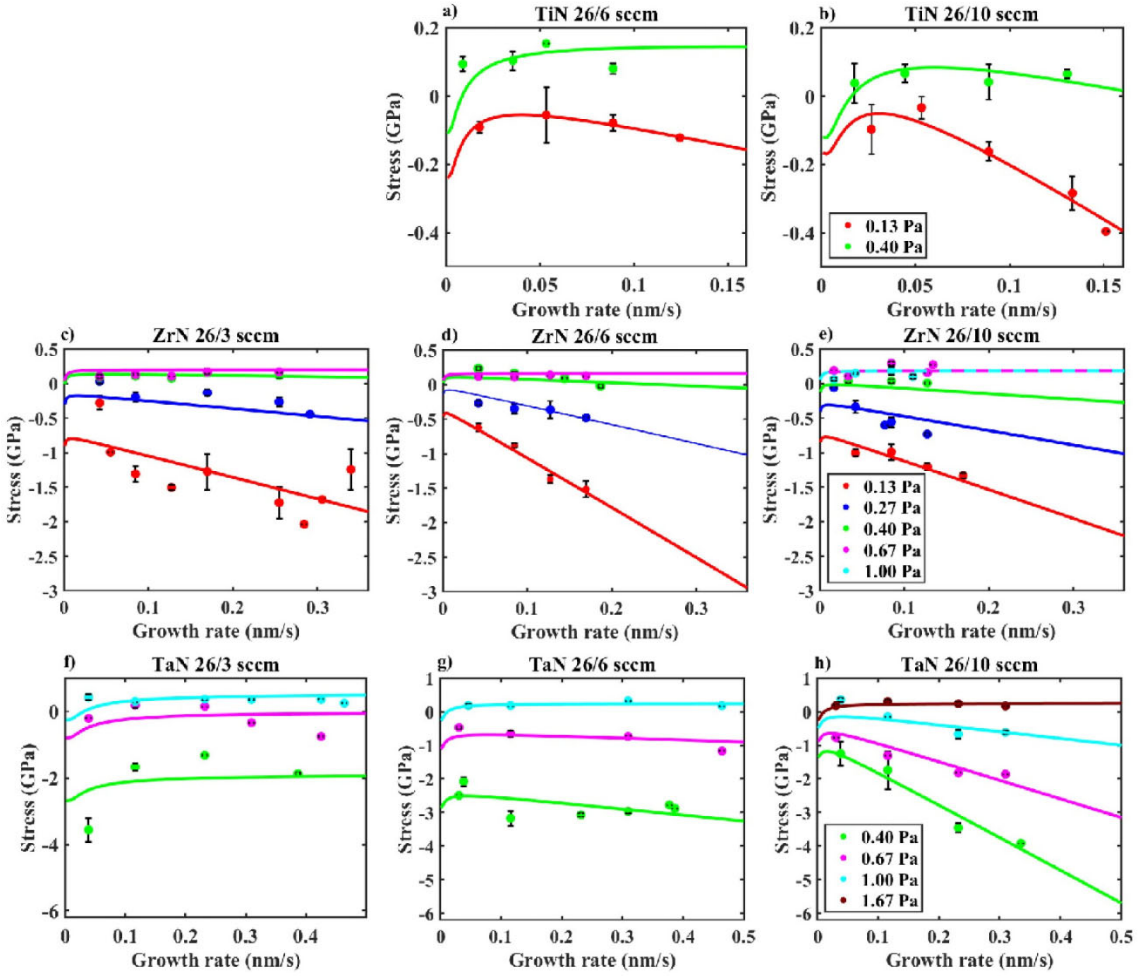

Fig. 2. Steady-state stress vs. growth rate for TiN a) 26/6 sccm, b) 26/10 sccm, ZrN c) 26/3 sccm, d) 26/6 sccm, e) 26/10 sccm, and TaN f) 26/3 sccm, g) 26/6 sccm and h) 26/10 sccm at different pressures. Solid lines are results of fitting to model.

the peak around 2θ = 33.203° in TiN, ZrN and TaN films belong to Si {002}. From the results, we can observe that the TiN and ZrN films exhibits the cubic rocksalt structure within the investigated processing conditions, and the intensity of peak {111} is stronger than that of {002}. In TaN films, all the films exhibit cubic δ-TaN structure. A hexagonal Ta_2N phase was detected at the lower gas flow rate of 26/3 sccm Ar/N_2 as shown in the asymmetric peak ranging from 34° to 40°. With an increase of the N_2 gas flow rate, the hexagonal-Ta_2N phase is no longer present. Formation of the hexagonal Ta_2N phase at lower N_2 gas flow rates has also been observed in the work from Zaman et al. [10] and Shin et al. [51]. Although the peak position is expected to change due to stress in the films, the XRD measurements are not precise enough to observe this correlation.

4. Discussion

4.1. Dependence on processing conditions

Several general observations can be made about the dependence of the stress on growth rate, flow rate ratio and pressure in each material. At the higher pressures, the dependence on the growth rate is weak, which is similar to the stress behavior in sputtered Mo [52] which also has low atomic mobility. In the low-pressure regime, the stress generally becomes more compressive at higher growth rates. For TiN and ZrN films, this has a weak dependence on the gas flow rate, whereas in sputtered TaN films, the stress is more compressive at higher N_2 flow rate in the high growth rate regime. In the following sections, we use the analytical model to analyze the data and discuss the meaning of the parameters obtained from fitting the data to the kinetic model.

4.2. Results of fitting to the stress model

To compare the experimental results with the kinetic model, a non-linear least square fitting routine was used to obtain the optimal fitting results by a minimization of the residual between the measured stress and the calculated stress from the kinetic model. The model parameters are described in Section 4.1. During the fitting, the parameters σ_c, σ_T, βD, D_i are assumed to be independent of processing conditions so that a single value of each was used to fit all the stress data in each material [44]. A_0, B_0, l can be different for different values of the pressure and gas flow rate ratios. In order to reduce the number of fitting parameters, A_0, B_0, l are assumed to have a linear dependence on pressure so that $A_0 = \left(1 - \frac{P}{P_0}\right)A^*$, $B_0 = \left(1 - \frac{P}{P_0}\right)B^*$, $l = \left(1 - \frac{P}{P_0}\right)l^*$ where P_0 is a threshold pressure at which the energetic effects are assumed to be negligible in each material. If the pressure is greater than P_0, these parameters are set to zero. The fitting parameter for the grain size, L, is assumed to have a constant value for each sequence of measurements at different growth rates (as in Fig. 1), but the value is allowed to be different for each pressure, flow rate ratio and material. Based on the TEM measurements, L was constrained in the fitting so that its value was limited to the range of 0–25 nm. Without this constraint, the largest fitting value for the grain size was 40 nm.

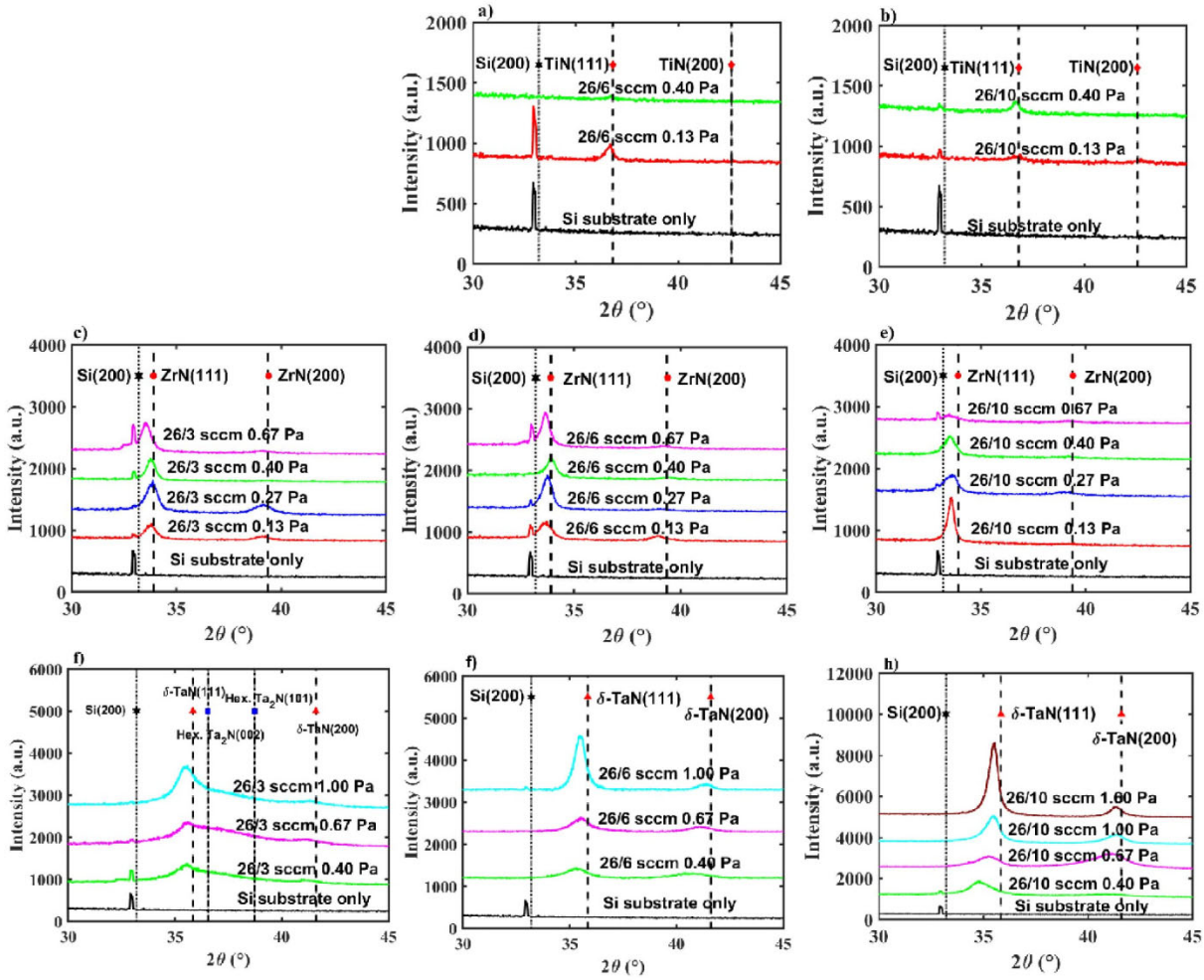

Fig. 3. XRD patterns for TiN a) 26/6 sccm, b) 26/10 sccm, ZrN c) 26/3 sccm, d) 26/6 sccm, e) 26/10 sccm, and TaN f) 26/3 sccm, g) 26/6 sccm and h) 26/10 sccm deposited with multiple growth rates at different pressures.

Table 3
Fitting parameters determined from the kinetic model. a) fitting parameters common to all processing conditions (σ_C, σ_T, βD, D_i) for TiN, ZrN and TaN. b) fitting parameters (A^*, B^*, l^*, P_0, L) at different pressure and gas flow rate ratio for TiN, ZrN and TaN.

a)

	σ_C (GPa)	$\sigma_T(L = 10nm)$ (GPa)	βD (nm^2/s)	D_i (nm^2/s)
TiN	−0.10	0.29	0.20	3.00
ZrN	0.00	0.25	0.03	7.91
TaN	−0.25	0.41	0.20	13.86

b)

	Flow rate (sccm)	P_0 (Pa)	L (nm)	A^* (GPa)	B^* (GPa)	l^* (nm)
TiN	26/6	0.50	13.4	−28.1	−27.7	0.23
	26/10	0.76	25.0	−2.0	−25.2	0.60
	26/3	0.48	15.8	−120.3	−200.0	0.23
ZrN	26/6	0.49	18.7	−44.0	−195.5	0.53
	26/10	0.61	25.0	−51.3	−101.2	0.53
	26/3	0.91	5.7	−1000.0	−0.3	0.04
TaN	26/6	1.03	25.0	−574.3	−222.3	0.30
	26/10	1.51	25.0	−194.6	−973.2	0.26

The resulting fitting values for σ_c, σ_T, βD, D_i for each material are shown in Table 3a. The fitting values for A^*, B^*, l^*, P_0 and L for each material and gas flow rate ratio is shown in Table 3b. The stresses calculated from the model using these parameters are shown as the solid lines in Fig. 2.

4.3. Discussion of the fitting parameters

Comparison of the data with the calculated stress in Fig. 2 suggests that the model is able to account for the dependence on the processing conditions for each material. As discussed in ref. [44], the fitting produces a reasonable set of values for the parameters, but their values should not be taken as unique, absolute minima of the mean-squared difference. This is because of several effects including physical approximations that make the model imperfect, experimental errors in the data and the broad minimum in parameter space. As a result, multiple sets of parameters can produce a similar quality of fit. Although their values may not be exact, insight can still be gained by a study of the dependence of the parameters on processing conditions and by a comparison with values expected from other measurements and calculations.

For each material, A_0 and B_0 vs. pressure are shown in Fig. 4, calculated from the fitting parameters A^*, $B^*$and P_0. The values in the figure are averaged over the results for the multiple flow rate ratios. The color corresponds to the different materials shown in the legend and the solid and dashed lines correspond to A_0 and B_0, respectively. Note that the linear dependence on pressure above P_0 is assumed in the fitting. The parameters for each material are found to be generally in the order TaN>ZrN > TiN.

For comparison, calculations were made using Monte-Carlo

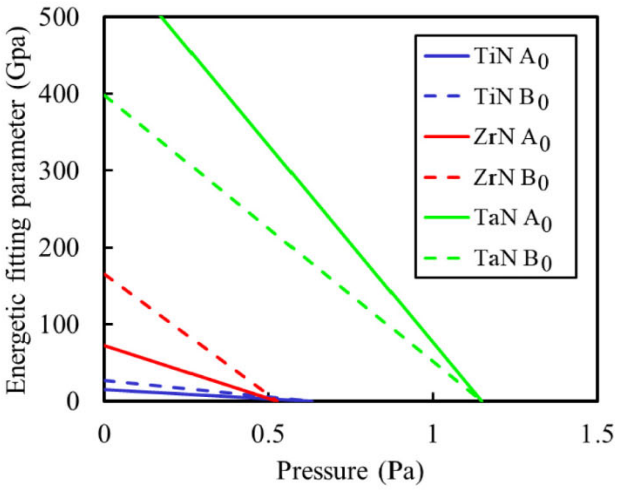

Fig. 4. Values of fitting parameters A_0 and B_0 averaged over the flow rates vs pressure for each material as indicated in the legend.

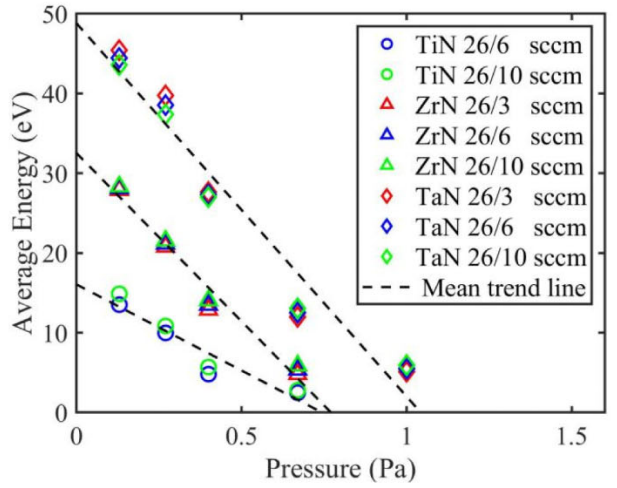

Fig. 5. Average energy per particle vs. pressure estimated by using SRIM and SIMTRA for TiN, ZrN and TaN at different pressures and gas flow rates.

simulations (SRIM and SIMTRA) to estimate the energy dependence of the stress-inducing particles. The average energy per sputtered atom arriving at the substrate is shown in Fig. 5 versus pressure for different materials and flow rate ratios indicated in the legend. The dashed line is a linear fit for each material averaged over all the flow rate ratios. For each material and flow rate ratio, the average energy decreases with the increase of pressure; the dashed line shows the results of a linear fit. This linearity supports the dependence of the energetic parameters A_0, B_0, l on pressure that is assumed in the fitting of the kinetic model.

The results of the calculations indicate that the average energy does not depend significantly on the ratio of the gas flow rate of Ar to N_2. This is consistent with the experimental results for TiN and ZrN in which the stress vs. growth rate has a weak dependence on the different gas flow rates. However, this does not explain why there is a greater flow rate dependence observed in TaN. As mentioned above, this may be related to effects of target poisoning that change the ratio of energetic to deposited species for different conditions. The more tensile stress at lower N_2 flow rates in TaN might also be due to the formation of N vacancies [53,54] as indicated by the formation of the hexagonal Ta_2N phase at lower N_2 flow rate from the XRD results.

The threshold pressure is the pressure at which the energetic effects become negligible, which can be estimated by taking the intercept of the linear fit of the average energy with the pressure axis (dashed line in Fig. 5). The estimates from the average energy fits have a larger intercept value for TaN and are similar for ZrN and TiN. This is similar to the trends in the average threshold pressure, P_0, obtained from the fitting shown in Fig. 4.

Table 4
Calculated implantation depth in nitride films at each pressure and gas flow rate ratio by using SRIM and SIMTRA.

	Pressure (Pa)	26/3 sccm	26/6 sccm	26/10 sccm
TiN	0.13	n/a	0.30 nm	0.30 nm
	0.40	n/a	0.27 nm	0.27 nm
ZrN	0.13	0.43 nm	0.43 nm	0.47 nm
	0.27	0.37 nm	0.40 nm	0.40 nm
	0.40	0.33 nm	0.37 nm	0.37 nm
	0.67	0.27 nm	0.30 nm	0.23 nm
TaN	0.40	0.47 nm	0.50 nm	0.53 nm
	0.67	0.37 nm	0.40 nm	0.43 nm
	1.00	0.30 nm	0.30 nm	0.33 nm

The implantation depth in TiN, ZrN and TaN is calculated by taking the weighted average of implantation depth from each energetic particle species in SRIM by using the average energy of each species generated from SIMTRA as input. The calculated implantation depth at each pressure and each gas flow rate ratio in each material was tabulated in Table 4. It indicates that the implantation depth is weakly dependent on the gas flow rate ratio, and it decreases with the increase of pressure. This trend is consistent with the fitting values obtained from the kinetic model, although the fitting predicts smaller values than the calculations.

The fitting parameter D_i in this study estimates an effective defect diffusivity in the material, but does not identify the origin of the diffusing defects or species. The value of D_i from the kinetic model for TiN, ZrN and TaN are 3.00, 7.91, and 13.86 nm^2/s, respectively. This is similar to the value of D_i in sputtered Mo [28] which is 7.2 nm^2/s. But much smaller than the predicted D_i for sputtered Cu [13] which is 5503.14 nm^2/s. The larger D_i in sputtered Cu indicates that fewer defects are incorporated in the films because of the higher defect diffusivity, leading to a lower compressive stress in sputtered Cu.

The parameter βD is related to the rate at which atoms can diffuse into the grain boundary to induce compressive stress. Its effect is evident in the transition from tensile to compressive stress when the growth rate is decreased [31] for materials with relatively high atomic mobility. For the nitrides, the atomic mobility is low so that this effect cannot be seen in the measurements. Rather, the dominant effect of growth rate is due to the trapping of defects as modeled by the B_0 term in Eq. (3). Therefore, the value of the βD parameter determined from the fitting is not reliable. Similarly good fits can be obtained if the βD parameter is constrained to have a much smaller value than shown in the table.

The parameters obtained from the fitting can also be compared with values estimated from other approaches. In the Hoffman mechanism [37], the tensile stress parameter σ_T is assumed to be proportional to $\sqrt{M_f \Delta\gamma / L}$ where M_f is the biaxial modulus and $\Delta\gamma$ is the interfacial energy difference between the free surface and the grain boundary based on the tensile stress mechanism proposed by Hoffman [37]. To estimate its value, $\Delta\gamma$ was taken to be proportional to the melting temperature of the material (3220, 3225, and 3360 K for TiN, ZrN and TaN, respectively) and the Young's moduli and Poisson's ratio are 440 GPa and 0.25 [55] for TiN, 400 GPa and 0.25 [56] for ZrN, and 383.8 GPa and 0.335 [57] for TaN. A plot of σ_T vs. $\sqrt{M_f T_M}$ at the same grain size of 1 nm is shown in Fig. 6. The data are consistent with the Hoffman model, although the range of measurements is too small to confirm the predicted dependence. For comparison, a linear correlation was also observed between σ_T and $\sqrt{M_f T_M}$ for evaporated metals [44]. The results for the metal-nitrides are smaller than what would be expected from extrapolation of the evaporated metal results.

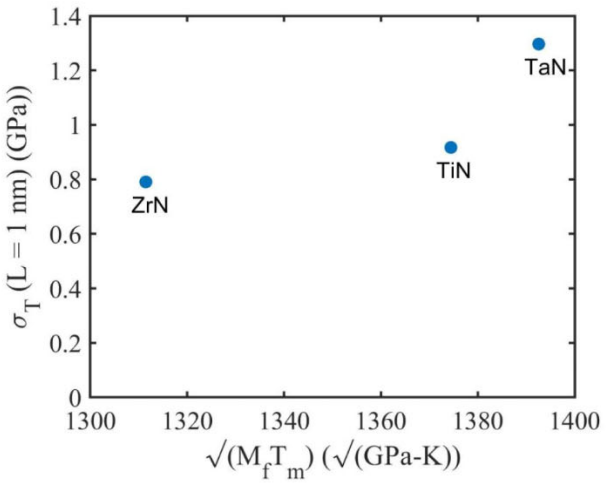

Fig. 6. Fitting-determined tensile stress parameter σ_T evaluated at L = 1 nm vs. the square root of the product of film modulus and melting temperature for each nitride film.

5. Conclusions

A series of experiments were conducted to investigate the effect of growth rate, pressure and gas flow rate ratio on stress in sputtered TiN, ZrN and TaN films. The processing parameters were varied systematically so that a steady-state stress could be associated with each set of growth conditions and associated grain size. The results, presented in a series of plots showing stress vs. growth rate for different materials, pressures and flow rate ratios, reveal trends in the data. For example, the stress is generally more compressive at lower pressure and more tensile at higher pressure. The compressive stress magnitude shows the trend that TiN < ZrN < TaN at lower pressure. The dependence on the ratio of Ar/N_2 gas flow rate is weak in TiN and ZrN, while higher relative N_2 flow in TaN tends to make the stress more compressive. The measurements are interpreted in terms of a previously developed kinetic model. The ability of the model to fit the data with a limited set of parameters supports the validity of the mechanisms used to simulate the effects of growth kinetics and energetic bombardment. Furthermore, the parameters obtained from fitting the model to the data are found to be consistent with calculations from Monte-Carlo simulations (SRIM and SIMTRA) for the energy of the incoming particles. By using this model, the connection between the stress, processing conditions and the underlying physical kinetic mechanisms is better understood. In addition, the fitting parameters obtained from this study can be used to predict the stress under different conditions or optimize the growth conditions for a desired stress.

CRediT authorship contribution statement

Zhaoxia Rao: Methodology, investigation, data analysis, writing-original draft, review & editing.

Tong Su: Data analysis, review & editing.

Thmoas Koenig: TEM observation, review & editing.

Gregory B. Thompson: Review & editing.

Diederik Depla: Review & editing.

Eric Chason: Conceptualization, methodology, investigation, supervision, review & editing, funding acquisition.

Declaration of competing interest

The authors declare that they have no known competing financial interests or personal relationships that could have appeared to influence the work reported in this paper.

Data availability

Data will be made available on request.

Acknowledgements

This work was supported by the National Science Foundation (NSF) under Contracts No. DMR-1602491 and DMR-2006422.

Appendix A. Supplementary data

Supplementary data to this article can be found online at https://doi.org/10.1016/j.surfcoat.2022.128880.

References

[1] S.Q. Wang, I. Raaijmakers, B.J. Burrow, S. Suthar, S. Redkar, K.B. Kim, Reactively sputtered TiN as a diffusion barrier between cu and si, J. Appl. Phys. 68 (1990) 5176–5187.
[2] M.B. Takeyama, A. Noya, K. Sakanishi, Diffusion barrier properties of ZrN films in the Cu/Si contact systems, J. Vac. Sci. Technol. B 18 (2000) 1333–1337.
[3] J.-S. Chun, I. Petrov, J.E. Greene, Dense fully 111-textured TiN diffusion barriers: enhanced lifetime through microstructure control during layer growth, J. Appl. Phys. 86 (1999) 3633–3641.
[4] A.E. Kaloyeros, E. Eisenbraun, Ultrathin diffusion Barriers/Liners for gigascale copper metallization, Annu. Rev. Mater. Sci. 30 (2000) 363–385.
[5] A.J. Perry, The state of residual stress in TiN films made by physical vapor deposition methods; the state of the art, J. Vac. Sci. Technol. A 8 (1990) 1351–1358.
[6] J.A. Thornton, D.W. Hoffman, Stress-related effects in thin films, Thin Solid Films 171 (1989) 5–31.
[7] Z. Rao, E. Chason, Measurements and modeling of residual stress in sputtered TiN and ZrN: dependence on growth rate and pressure, Surf. Coat. Technol. 404 (2020), 126462.
[8] L.E. Koutsokeras, G. Abadias, Intrinsic stress in ZrN thin films: evaluation of grain boundary contribution from in situ wafer curvature and ex situ x-ray diffraction techniques, J. Appl. Phys. 111 (2012), 093509.
[9] G. Abadias, L.E. Koutsokeras, A. Siozios, P. Patsalas, Stress, phase stability and oxidation resistance of ternary Ti–Me–N (Me=Zr, Ta) hard coatings, Thin Solid Films 538 (2013) 56–70.
[10] A. Zaman, E.I. Meletis, Microstructure and mechanical properties of TaN thin films prepared by reactive magnetron sputtering, Coatings 7 (2017) 209.
[11] J.-H. Huang, C.-H. Ho, G.-P. Yu, Effect of nitrogen flow rate on the structure and mechanical properties of ZrN thin films on Si(100) and stainless steel substrates, Mater. Chem. Phys. 102 (2007) 31–38.
[12] G. Abadias, W.P. Leroy, S. Mahieu, D. Depla, Influence of particle and energy flux on stress and texture development in magnetron sputtered TiN films, J. Phys. D. Appl. Phys. 46 (2012), 055301.
[13] T. Kaub, Z. Rao, E. Chason, G.B. Thompson, The influence of deposition parameters on the stress evolution of sputter deposited copper, Surf. Coat. Technol. 357 (2019) 939–946.
[14] H.Y. Liu, G.S. Tang, F. Zeng, F. Pan, Influence of sputtering parameters on structures and residual stress of AlN films deposited by DC reactive magnetron sputtering at room temperature, J. Cryst. Growth 363 (2013) 80–85.
[15] K. Kusaka, D. Taniguchi, T. Hanabusa, K. Tominaga, Effect of input power on crystal orientation and residual stress in AlN film deposited by dc sputtering, Vacuum 59 (2000) 806–813.
[16] A. Jamnig, N. Pliatsikas, K. Sarakinos, G. Abadias, The effect of kinetics on intrinsic stress generation and evolution in sputter-deposited films at conditions of high atomic mobility, J. Appl. Phys. 127 (2020), 045302.
[17] Y.G. Shen, Effect of deposition conditions on mechanical stresses and microstructure of sputter-deposited molybdenum and reactively sputter-deposited molybdenum nitride films, Mater. Sci. Eng. A 359 (2003) 158–167.
[18] C.T. Wu, Intrinsic stress of magnetron-sputtered niobium films, Thin Solid Films 64 (1979) 103–110.
[19] J.A. Thornton, J. Tabock, D.W. Hoffman, Internal stresses in metallic films deposited by cylindrical magnetron sputtering, Thin Solid Films 64 (1979) 111–119.
[20] E.A.I. Ellis, M. Chmielus, S.P. Baker, Effect of sputter pressure on ta thin films: Beta phase formation, texture, and stresses, Acta Mater. 150 (2018) 317–326.
[21] A.J. Detor, A.M. Hodge, E. Chason, Y. Wang, H. Xu, M. Conyers, A. Nikroo, A. Hamza, Stress and microstructure evolution in thick sputtered films, Acta Mater. 57 (2009) 2055–2065.
[22] G. Abadias, L.E. Koutsokeras, P. Guerin, P. Patsalas, Stress evolution in magnetron sputtered Ti–Zr–N and Ti–Ta–N films studied by in situ wafer curvature: role of energetic particles, Thin Solid Films 518 (2009) 1532–1537.
[23] J. Lin, W.D. Sproul, J.J. Moore, Z.L. Wu, S.L. Lee, Effect of negative substrate bias voltage on the structure and properties of CrN films deposited by modulated pulsed power (MPP) magnetron sputtering, J. Phys. D. Appl. Phys. 44 (2011), 425305.

[24] H.-C. Lee, J.-Y. Lee, H.-J. Ahn, Effect of the substrate bias voltage on the crystallographic orientation of reactively sputtered AlN thin films, Thin Solid Films 251 (1994) 136–140.
[25] A.M. Engwall, S.J. Shin, J. Bae, Y.M. Wang, Enhanced properties of tungsten films by high-power impulse magnetron sputtering, Surf. Coat. Technol. 363 (2019) 191–197.
[26] F. Cemin, G. Abadias, T. Minea, C. Furgeaud, F. Brisset, D. Solas, D. Lundin, Benefits of energetic ion bombardment for tailoring stress and microstructural evolution during growth of cu thin films, Acta Mater. 141 (2017) 120–130.
[27] D. Magnfält, A. Fillon, R.D. Boyd, U. Helmersson, K. Sarakinos, G. Abadias, Compressive intrinsic stress originates in the grain boundaries of dense refractory polycrystalline thin films, J. Appl. Phys. 119 (2016), 055305.
[28] E. Chason, M. Karlson, J.J. Colin, D. Magnfält, K. Sarakinos, G. Abadias, A kinetic model for stress generation in thin films grown from energetic vapor fluxes, J. Appl. Phys. 119 (2016), 145307.
[29] J.F. Ziegler, J.P. Biersack, U. Littmark, The Stopping and Range of Ions in Matter, Springer, Boston, MA, 1985.
[30] K. Van Aeken, S. Mahieu, D. Depla, The metal flux from a rotating cylindrical magnetron: a Monte Carlo simulation, J. Phys. D. Appl. Phys. 41 (2008), 205307.
[31] E. Chason, P.R. Guduru, Tutorial: understanding residual stress in polycrystalline thin films through real-time measurements and physical models, J. Appl. Phys. 119 (2016), 191101.
[32] L.B. Freund, S. Suresh, Thin Film Materials: Stress, Defect Formation and Surface Evolution, Cambridge University Press, Cambridge, 2004.
[33] G.G. Stoney, The tension of metallic films deposited by electrolysis, Proc. Math. Phys. Eng. Sci. 82 (1909) 172–175.
[34] G. Abadias, P. Guerin, In situ stress evolution during magnetron sputtering of transition metal nitride thin films, Appl. Phys. Lett. 93 (2008), 111908.
[35] Z. Rao, S.J. Hearne, E. Chason, The effects of plating current, grain size, and electrolyte on stress evolution in electrodeposited ni, J. Electrochem. Soc. 166 (2018) D3212–D3218.
[36] E. Chason, B.W. Sheldon, L.B. Freund, J.A. Floro, S.J. Hearne, Origin of compressive residual stress in polycrystalline thin films, Phys. Rev. Lett. 88 (2002), 156103.
[37] R.W. Hoffman, Stresses in thin films: the relevance of grain boundaries and impurities, Thin Solid Films 34 (1976) 185–190.
[38] E. Chason, A kinetic analysis of residual stress evolution in polycrystalline thin films, Thin Solid Films 526 (2012) 1–14.
[39] A.M. Engwall, Z. Rao, E. Chason, Origins of residual stress in thin films: interaction between microstructure and growth kinetics, Mater. Des. 110 (2016) 616–623.
[40] A.M. Engwall, Z. Rao, E. Chason, Residual stress in electrodeposited cu thin films: understanding the combined effects of growth rate and grain size, J. Electrochem. Soc. 164 (2017) D828–D834.
[41] E. Chason, A. Engwall, F. Pei, M. Lafouresse, U. Bertocci, G. Stafford, J.A. Murphy, C. Lenihan, D.N. Buckley, Understanding residual stress in electrodeposited cu thin films, J. Electrochem. Soc. 160 (2013) D3285–D3289.
[42] V.P. Graciano, U. Bertocci, G.R. Stafford, In-situ stress measurements during cobalt electrodeposition, J. Electrochem. Soc. 166 (2019) D3246–D3253.
[43] E. Chason, A.M. Engwall, Z. Rao, T. Nishimura, Kinetic model for thin film stress including the effect of grain growth, J. Appl. Phys. 123 (2018), 185305.
[44] Z. Rao, S. Berman, P. Yang, D. Depla, E. Chason, Understanding residual stress in thin films: analyzing wafer curvature measurements for ag, cu, ni, fe, ti, and cr with a kinetic model, J. Appl. Phys. 130 (2021), 135304.
[45] D. Magnfalt, G. Abadias, K. Sarakinos, Atom insertion into grain boundaries and stress generation in physically vapor deposited films, Appl. Phys. Lett. 103 (2013).
[46] T.R. Koenig, Z. Rao, E. Chason, G.J. Tucker, G.B. Thompson, The microstructural and stress evolution in sputter deposited ni thin films, Surf. Coat. Technol. 412 (2021), 126973.
[47] G. Abadias, E. Chason, J. Keckes, M. Sebastiani, G.B. Thompson, E. Barthel, G. L. Doll, C.E. Murray, C.H. Stoessel, L. Martinu, Review article: stress in thin films and coatings: current status, challenges, and prospects, J. Vac. Sci. Technol. A 36 (2018), 020801.
[48] S. Mahieu, K. Van Aeken, D. Depla, Quantification of the ion and momentum fluxes toward the substrate during reactive magnetron sputtering, J. Appl. Phys. 104 (2008).
[49] A. Bogaerts, I. Kolev, G. Buyle, Modeling of the magnetron discharge, in: D. Depla, S. Mahieu (Eds.), Reactive Sputter Deposition, Springer, Berlin, 2008.
[50] P. Lucasson, Fundamental aspects of radiation damage in metals, in: Proceedings of International Conference at Gatlinburg, 1975, p. 4.
[51] C.-S. Shin, Y.-W. Kim, N. Hellgren, D. Gall, I. Petrov, J.E. Greene, Epitaxial growth of metastable δ-TaN layers on MgO(001) using low-energy, high-flux ion irradiation during ultrahigh vacuum reactive magnetron sputtering, J. Vac. Sci. Technol. A 20 (2002) 2007–2017.
[52] A. Fillon, G. Abadias, A. Michel, C. Jaouen, Stress and microstructure evolution during growth of magnetron-sputtered low-mobility metal films: influence of the nucleation conditions, Thin Solid Films 519 (2010) 1655–1661.
[53] N. Koutna, D. Holec, O. Svoboda, F.F. Klimashin, P.H. Mayrhofer, Point defects stabilise cubic mo-N and ta-N, J. Phys. D. Appl. Phys. 49 (2016).
[54] G. Abadias, C.H. Li, L. Belliard, Q.M. Hu, N. Greneche, P. Djemia, Large influence of vacancies on the elastic constants of cubic epitaxial tantalum nitride layers grown by reactive magnetron sputtering, Acta Mater. 184 (2020) 254–266.
[55] D.S. Stone, K.B. Yoder, W.D. Sproul, Hardness and elastic modulus of TiN based on continuous indentation technique and new correlation, J. Vac. Sci. Technol. A 9 (1991) 2543–2547.
[56] E. Török, A.J. Perry, L. Chollet, W.D. Sproul, Young's modulus of TiN, TiC, ZrN and HfN, Thin Solid Films 153 (1987) 37–43.
[57] J. Chang, G.-P. Zhao, X.-L. Zhou, K. Liu, L.-Y. Lu, Structure and mechanical properties of tantalum mononitride under high pressure: a first-principles study, J. Appl. Phys. 112 (2012), 083519.